Local nonequilibrium dissipation scaling in compressible homogeneous isotropic turbulence

Yohei Nishimoto (西本洋平), Koji Nagata (長田孝二),[a] and Tomoaki Watanabe (渡邉智昭)

Department of Mechanical Engineering and Science, Kyoto University, Kyoto 615-8530, Japan

(Dated: 7 April 2026)

We quantify the nondimensional turbulent kinetic energy dissipation rate, C_ε, in compressible homogeneous isotropic turbulence using a direct numerical simulation (DNS) database sustained by solenoidal linear forcing. Integral-scale Reynolds numbers are $Re_{L0} = 140$, 350, and 900, corresponding to Taylor–microscale Reynolds numbers $Re_\lambda \simeq 40$–150, and the turbulent Mach number spans $M_{T0} = 0.3$–0.9 in each set. The velocity field is decomposed into solenoidal and dilatational components via the Helmholtz decomposition, and dissipation measures are evaluated consistently for each component. Global statistics of the nondimensional dissipation rate generally agree with those reported in previous studies. A subdomain-based analysis provides a local characterization of dissipation scaling in compressible isotropic turbulence. When conditioned on locally evaluated Re_λ, conditional averages of C_ε collapse across all cases and follow nonequilibrium scaling, $C_\varepsilon \sim Re_\lambda^{-1}$, and the solenoidal contribution obeys the same scaling, $C_{\varepsilon s} \sim Re_\lambda^{-1}$. In contrast, the dilatational contribution is only weakly dependent on local Re_λ and instead correlates with local compressibility, increasing monotonically with the dilatational turbulent Mach number. These results demonstrate that nonequilibrium dissipation is fundamentally local and that compressibility enters primarily through intermittent dilatational dynamics.

[a] Author to whom correspondence should be addressed: nagata.koji.2y@kyoto-u.ac.jp

Local nonequilibrium dissipation scaling in compressible homogeneous isotropic turbulence

I. INTRODUCTION

The dissipation rate of turbulent kinetic energy, ε, is a central quantity in turbulence and underpins modeling and prediction across a wide range of flows.[1] Under the equilibrium assumption that the interscale energy flux balances viscous dissipation, Kolmogorov[2–4] showed that the nondimensional dissipation rate,

$$C_\varepsilon = \frac{\varepsilon L}{u_{\rm rms}^3}, \tag{1}$$

approaches a constant, where $u_{\rm rms}$ is the root-mean-square (r.m.s.) velocity fluctuation and L is a characteristic large-eddy length scale, typically the integral length scale. Consistently, many studies report that C_ε becomes approximately independent of the turbulent Reynolds number $Re_\lambda = u_{\rm rms}\lambda/\nu$ at sufficiently high Reynolds numbers,[1,5–9] where λ is the Taylor microscale and ν is the kinematic viscosity. In contrast, nonequilibrium dissipation ($C_\varepsilon \neq$ const.) has also been observed,[1,10–13] motivating empirical and theoretical descriptions of nonequilibrium scaling.[1,11,14] More recently, Kitamura et al.[15] derived an exact relation between C_ε and an integrated form of the Kármán–Howarth equation for forced and decaying homogeneous isotropic turbulence (HIT), providing a rigorous framework for interpreting observed scalings.

While most evidence for nonequilibrium dissipation has been obtained in incompressible flows, compressibility introduces additional dynamics that can alter dissipation pathways. In compressible turbulence, velocity fluctuations can be decomposed into solenoidal (divergence-free) and dilatational (curl-free) components, and both contribute to kinetic-energy dissipation. John et al.[16] examined the corresponding nondimensional dissipation rates and showed that the solenoidal contribution behaves similarly to its incompressible counterpart: it tends toward an approximately constant value at sufficiently high Re_λ (with an improved collapse when a solenoidal Reynolds number is used), whereas a stronger Re_λ dependence remains at lower Re_λ. In contrast, the dilatational contribution does not exhibit a systematic collapse when plotted against Re_λ alone and becomes approximately constant only when the characteristic time scales of solenoidal and dilatational motions are comparable. From a scale-transfer perspective, Aluie[17] showed that interscale transfer of mean kinetic energy in compressible turbulence is dominated by scale-local interactions and, under an additional assumption on pressure dilatation, supports an inertial-range cascade with an

approximately constant mean kinetic-energy flux despite density fluctuations and compression/expansion effects. Consistent with this picture, Pearson et al.[18] demonstrated that in statistically stationary, isotropic box turbulence with random transverse (solenoidal) forcing and weak compressibility, the nondimensional dissipation rate based on the total velocity field approaches an approximately constant value at sufficiently high Re_λ. Moreover, Jagannathan and Donzis[19] reported a critical turbulent Mach number of $M_t \approx 0.3$ that separates two regimes and showed that the dilatational contribution to the normalized dissipation increases markedly (in relative importance) for $M_t \gtrsim 0.3$, highlighting compressibility effects beyond Reynolds-number dependence.

A key limitation of existing studies of compressible turbulence is that they primarily rely on global statistics, which can mask strong spatio-temporal intermittency. In incompressible grid turbulence, Zheng et al.[20,21] demonstrated that a local nondimensional dissipation rate (based on short-time averages) can follow nonequilibrium scaling even when the corresponding global value (based on long-time averages) is nearly Re_λ-independent. These results suggest that nonequilibrium behavior is fundamentally local and may not be detectable from global averages alone. Motivated by this insight, the present work provides, to our knowledge, the first local characterization of nondimensional dissipation in compressible turbulence. Using a direct numerical simulation (DNS) database of compressible HIT, we quantify C_ε for the total velocity field and for its solenoidal and dilatational components, both globally and locally. For the local analysis, the computational domain is partitioned into cubic subdomains with side length on the order of the integral length scale, and subdomain statistics are used to assess local dissipation scaling and its dependence on Reynolds number and turbulent Mach number. This local framework allows us to isolate how compressibility enters the dissipation dynamics and to determine whether nonequilibrium scaling persists at spatially local scales in compressible turbulence. Beyond the present dataset, this subdomain-based conditional framework is broadly applicable to turbulent flows in which strong spatio-temporal intermittency compromises the interpretability of long-time, whole-domain averages. By conditioning dissipation measures on the instantaneous local flow state, the approach (i) reduces scatter induced by global mixing of disparate local regimes, (ii) enables separate assessment of Reynolds-number and compressibility (Mach-number) effects within a unified similarity framework, and (iii) provides a practical route for comparing simulations and experiments on a common local basis. More generally, the same methodology

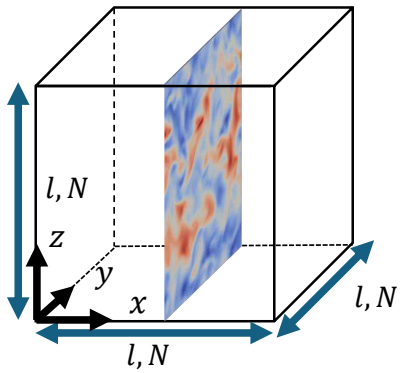

FIG. 1: Triply periodic computational domain and coordinate system.

can be used to interrogate scaling laws, quantify intermittency, and benchmark turbulence models whenever sufficiently resolved fields (or local measurements) are available.

The remainder of the paper is organized as follows: Sec. II describes the DNS database and the analysis procedure; Sec. III presents the results; and Sec. IV summarizes the conclusions.

II. DNS DATABASE AND ANALYSIS

A. DNS database of compressible HIT

This section summarizes the DNS database of compressible HIT sustained by solenoidal linear forcing; details of the numerical method and forcing strategy are provided in Refs. 22 and 23. Figure 1 shows the triply periodic cubic domain and the coordinate system used in the present work.

Statistical stationarity is achieved by applying linear forcing to the solenoidal component of the velocity field. In practice, additional forcing and cooling terms are included in the momentum and energy equations to maintain a statistically steady state. The governing equations are the nondimensional compressible Navier–Stokes equations with the perfect-gas equation of state:

$$\frac{\partial \rho}{\partial t} + \frac{\partial \rho u_j}{\partial x_j} = 0, \tag{2}$$

$$\frac{\partial \rho u_i}{\partial t} + \frac{\partial \rho u_i u_j}{\partial x_j} = -\frac{\partial P}{\partial x_i} + \frac{1}{Re}\frac{\partial \tau_{ij}}{\partial x_j} + f_i, \tag{3}$$

$$\frac{\partial \rho T}{\partial t} + \frac{\partial \rho T u_j}{\partial x_j} = -(\gamma - 1)P\frac{\partial u_j}{\partial x_j} + \frac{\gamma}{RePr}\frac{\partial}{\partial x_j}\left(\kappa \frac{\partial T}{\partial x_j}\right) + \frac{\gamma - 1}{Re}\tau_{ij}\frac{\partial u_i}{\partial x_j} + f_e, \tag{4}$$

$$P = \rho T, \tag{5}$$

where t is time, x_i is the ith spatial coordinate, ρ is density, u_i is the ith velocity component, P is pressure, T is temperature, $\gamma = 1.4$ is the ratio of specific heats, κ is the thermal conductivity, and τ_{ij} is the viscous stress tensor, given by

$$\tau_{ij} = \mu\left(\frac{\partial u_i}{\partial x_j} + \frac{\partial u_j}{\partial x_i} - \frac{2}{3}\delta_{ij}\frac{\partial u_k}{\partial x_k}\right), \tag{6}$$

where μ is the dynamic viscosity computed using Sutherland's law and δ_{ij} is the Kronecker delta. Repeated indices imply summation. The terms f_i and f_e represent the forcing and cooling contributions in the momentum and energy equations, respectively. The nondimensional control parameters are the Reynolds number $Re = \rho_r u_r l_r/\mu_r$ and the Prandtl number $Pr = \tilde{\mu}c_p/\tilde{\kappa} = 0.71$. Here, c_p is the specific heat capacity at constant pressure and $\tilde{\cdot}$ denotes a dimensional quantity and the subscript r indicates the reference values used for nondimensionalization.

The turbulent state is prescribed by four target parameters: the integral-scale Reynolds number Re_{L0}, the turbulent Mach number M_{T0}, and the mean thermodynamic quantities P_0 and T_0. Here, the subscript 0 denotes the target value in the statistically steady state. The parameters Re_{L0} and M_{T0} are defined as

$$Re_{L0} = \frac{\rho_0 u_0 L_0}{\mu_0};\ M_{T0} = \frac{\sqrt{3}u_0}{a_0}, \tag{7}$$

with u_0 the root-mean-square velocity fluctuation, $L_0 = u_0^3/\varepsilon_0$ the integral length scale (ε_0 is the dissipation rate per unit mass), and $a_0 = \sqrt{\gamma R T_0}$ the sound speed (R is the gas constant). The reference quantities used for normalization in Eqs. (2)–(5) are $l_r = L_0$, $u_r = u_0$, $\rho_r = \rho_0 = P_0/RT_0$, $\mu_r = \mu_0 = \tilde{\mu}(T_0)$, $\kappa_r = \mu_0 c_p/Pr$.

Table I summarizes the flow conditions, the domain side length, and the grid resolution N^3. Three Reynolds numbers, $Re_{L0} = 140$, 350, and 900, are considered. For each Re_{L0}, the turbulent Mach number is set to $M_{T0} = 0.3$, 0.5, 0.7, 0.8, and 0.9. The domain size is fixed at $l = 5.5L_0$ for all cases. We emphasize that L_0 is defined using the target dissipation rate per unit mass, ε_0, rather than the a posteriori dissipation rate obtained from the DNS. The

TABLE I: Flow parameters and numerical resolution for the DNS database of compressible HIT.[22,23]

Re_{L0}	M_{T0}	l	N^3
140	0.3, 0.5, 0.7, 0.8, 0.9	$5.5L_0$	385^3
350	0.3, 0.5, 0.7, 0.8, 0.9	$5.5L_0$	769^3
900	0.3, 0.5, 0.7, 0.8, 0.9	$5.5L_0$	1537^3

target velocity scale u_0 (and hence L_0) is determined a priori from the input parameters $(T_0, P_0, M_{T0}, Re_{L0})$ and the equation of state. The computational domain size is then set before running the DNS. Hereafter, figure captions specify the flow conditions using Re_L and M_t. For example, "$Re_L900M_t0.9$" indicates the case with $Re_{L0} = 900$ and $M_{T0} = 0.9$. This simplified notation is appropriate because, in the statistically steady state, the attained values satisfy $Re_L \approx Re_{L0}$ and $M_t \approx M_{T0}$.[22]

B. Helmholtz decomposition

We apply the Helmholtz decomposition to the velocity field $\boldsymbol{u}$, writing it as the sum of a solenoidal component $\boldsymbol{u}_s$ and a dilatational (irrotational) component $\boldsymbol{u}_d$. That is, $\boldsymbol{u} = \boldsymbol{u}_s + \boldsymbol{u}_d$, with $\nabla \cdot \boldsymbol{u}_s = 0$ and $\nabla \times \boldsymbol{u}_d = \boldsymbol{0}$.

Because $\boldsymbol{u}_d$ is irrotational, it can be expressed as the gradient of a scalar potential ϕ, i.e., $\boldsymbol{u}_d = \nabla\phi$. Taking the divergence of $\boldsymbol{u} = \boldsymbol{u}_s + \boldsymbol{u}_d$ and using $\nabla \cdot \boldsymbol{u}_s = 0$ yields the Poisson equation

$$\nabla^2\phi = \nabla \cdot \boldsymbol{u}. \tag{8}$$

Thus, ϕ is obtained by solving $\nabla^2\phi = \nabla \cdot \boldsymbol{u}$ (with the zero-mean mode set to ensure uniqueness in a periodic domain).

The solenoidal component can be represented using a vector potential $\boldsymbol{A}$ as $\boldsymbol{u}_s = \nabla \times \boldsymbol{A}$. Introducing the vorticity $\boldsymbol{\omega} = \nabla \times \boldsymbol{u}$ and using $\nabla \times \boldsymbol{u}_d = \boldsymbol{0}$ give

$$\nabla \times \boldsymbol{u}_s = \nabla \times \boldsymbol{u} = \boldsymbol{\omega}. \tag{9}$$

With the Coulomb gauge $\nabla \cdot \boldsymbol{A} = 0$, we obtain $\nabla \times (\nabla \times \boldsymbol{A}) = -\nabla^2\boldsymbol{A} = \boldsymbol{\omega}$, leading to the

Poisson equation

$$\nabla^2 \boldsymbol{A} = -\boldsymbol{\omega}. \tag{10}$$

In the triply periodic domain, the Poisson equations for ϕ and $\boldsymbol{A}$ are solved efficiently in Fourier space (with the zero-wavenumber mode handled to fix the arbitrary constant/gauge). The decomposed fields are then obtained as

$$\boldsymbol{u}_d = \nabla\phi, \qquad \boldsymbol{u}_s = \nabla \times \boldsymbol{A}. \tag{11}$$

C. Global and local scale analysis

To quantify dissipation scaling at spatially local scales—a central contribution of the present work—we perform a subdomain-based analysis of the DNS fields. For each (Re_{L0}, M_{T0}) case, the triply periodic computational domain is partitioned into non-overlapping cubic subdomains whose side length is set equal to the integral length scale L evaluated from statistics over the full domain. The subdomain side length is chosen to be of the order of the integral length scale, $\ell_{\mathrm{local}} \simeq L$, because L characterizes the energy-containing eddies. This choice provides a practical balance between spatial locality and statistical reliability: overly large subdomains smear out local variability of large-scale motions and approach global statistics, whereas overly small subdomains can suffer from insufficient convergence and may introduce artifacts. To assess sensitivity to the subdomain size, we note that in our previous grid-turbulence studies the main local scaling behavior was found to be essentially insensitive to ℓ_{local} over broad ranges: $0.3L \le \ell_{\mathrm{local}} \le 5L$ in wind-tunnel experiments[20] and $0.5L \le \ell_{\mathrm{local}} \le 2L$ in DNS.[24] Accordingly, the choice $\ell_{\mathrm{local}} \simeq L$ adopted here is expected to be robust, at least for nearly homogeneous isotropic turbulence where L provides a natural outer scale for local averaging. Within each subdomain, we compute local statistics, including the nondimensional dissipation rate C_ε, the turbulent Reynolds number Re_λ, and the turbulent Mach number M_t. We then evaluate conditional averages of these quantities conditioned on the local value of Re_λ, which enables us to assess whether global scalings persist locally and to isolate the effects of intermittency. In practice, to ensure adequate sampling for conditional averaging, the range between the minimum and maximum local values of Re_λ in each case is divided into 25 logarithmically spaced bins, and ensemble averages are computed within each bin. A bin is retained only if it contains at least 1/100

of the total number of subdomains; bins with fewer samples are excluded from the plots to reduce statistical uncertainty. Throughout this paper, statistics computed over the entire domain are referred to as "global", whereas those computed within subdomains are referred to as "local".

Following Watanabe et al.,[25] we define the integral length scale L from the second-order structure function using the area-preserving representation of its gradient. We adopt this definition instead of the more conventional integral length scale obtained from the integral of the longitudinal two-point autocorrelation function, because in some of our cases the autocorrelation does not decay to (or sufficiently close to) zero even at large r. In such situations, the correlation-based integral length scale becomes sensitive to finite-domain effects and the choice of integration cutoff, and can therefore be ill-defined or poorly converged. In practice, we evaluate the longitudinal second-order structure functions along the x, y, and z directions using the corresponding velocity components,

$$\left\langle (\Delta_r u_j)^2 \right\rangle = \left\langle \left(u_j(\boldsymbol{x} + r\boldsymbol{e}_j) - u_j(\boldsymbol{x})\right)^2 \right\rangle, \ (u_x, u_y, u_z) = (u, v, w), \quad j \in \{x, y, z\}, \tag{12}$$

where r is the separation distance, $\boldsymbol{e}_j$ is the unit vector in direction j, and $\langle\cdot\rangle$ denotes an ensemble average. We then compute the derivative $\mathrm{d}\langle(\Delta_r u_j)^2\rangle/\mathrm{d}r$ and determine the integral length as the values of r at which the area-preserving form

$$r \frac{\mathrm{d}}{\mathrm{d}r} \left\langle (\Delta_r u_j)^2 \right\rangle \tag{13}$$

attains its maximum when plotted against $\log r$ (i.e., in semi-log coordinates). The integral length scale is then defined as the average

$$L = \frac{1}{3} \left(L_x + L_y + L_z\right), \tag{14}$$

where L_j denotes the integral length scale computed with the structure function of u_j. The solenoidal and dilatational integral length scales, L_s and L_d, are defined analogously using the corresponding solenoidal and dilatational velocity components.

The Taylor microscale is calculated as

$$\lambda_j = \frac{u_{j,\mathrm{rms}}}{\sqrt{\left\langle (\partial u_j/\partial x_j)^2 \right\rangle}} \text{ (no summation over } j), \ (u_{x,\mathrm{rms}}, u_{y,\mathrm{rms}}, u_{z,\mathrm{rms}}) = (u_{\mathrm{rms}}, v_{\mathrm{rms}}, w_{\mathrm{rms}}), \tag{15}$$

$$\lambda = \frac{1}{3} \left(\lambda_x + \lambda_y + \lambda_z\right). \tag{16}$$

Here, the r.m.s. value of a quantity f is computed as $f_{\rm rms} = \sqrt{\langle f^2 \rangle - \langle f \rangle^2}$.

The global length scales are computed in the same manner. We, however, restrict the evaluation of the integral length scales in the global scale to the y and z directions (i.e., $L = (L_y + L_z)/2$) for computational convenience: in our MPI implementation, the domain is decomposed along x. We confirmed that, at the global scale, $L_y/L_z \sim L_{sy}/L_{sz} \sim L_{dy}/L_{dz} \sim 1.0$, where L_{sy} and L_{sz} (L_{dy} and L_{dz}) denote the solenoidal (dilatational) integral length scales in the y and z directions, respectively.

The mean dissipation rate per unit mass is computed as

$$\varepsilon = \langle \tau_{ij} s_{ij} / Re \rangle \, / \, \langle \rho \rangle \,, \tag{17}$$

where $s_{ij} = \frac{1}{2} \left(\partial u_i / \partial x_j + \partial u_j / \partial x_i \right)$ is the strain-rate tensor. Then, C_ε is computed by

$$C_\varepsilon = \frac{\varepsilon L}{u_{k,\rm rms}^3}, \tag{18}$$

where $u_{k,\rm rms}$ is the r.m.s. velocity defined with

$$u_{k,\rm rms} = \sqrt{\frac{1}{3}(u_{\rm rms}^2 + v_{\rm rms}^2 + w_{\rm rms}^2)}. \tag{19}$$

The turbulent Reynolds number is calculated by

$$Re_\lambda = \frac{\langle \rho \rangle u_{k,\rm rms} \lambda}{\langle \mu \rangle} Re, \tag{20}$$

and the turbulent Mach number by

$$M_t = \frac{\sqrt{3} u_{k,\rm rms}}{\sqrt{\gamma \langle T \rangle}}. \tag{21}$$

III. RESULTS AND DISCUSSION

A. Global Statistics

1. Energy spectrum

Figure 2 shows the one-dimensional (longitudinal) energy spectrum of the z-velocity component, w, denoted by $E_{ww}(k_z)$. Here, $\eta = (\nu^3/\varepsilon)^{1/4}$ and $u_\eta = (\nu\,\varepsilon)^{1/4}$ are the Kolmogorov length and velocity scales, respectively, and k_z is the z component of the wavenumber vector. In HIT, spectra are often reported as the isotropically averaged three-dimensional spectrum $E(k)$ with $k = \sqrt{k_x^2 + k_y^2 + k_z^2}$ (k_x, k_y, and k_z are the x, y, and z components of

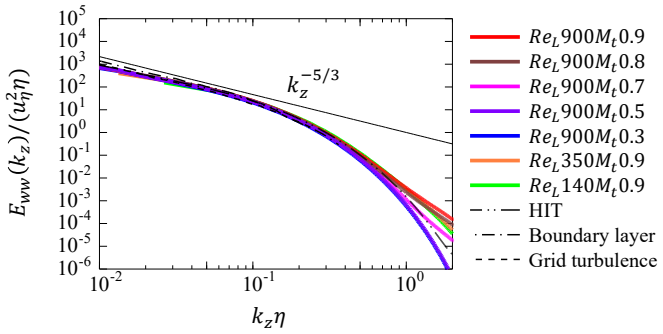

FIG. 2: One-dimensional longitudinal energy spectrum of the z-velocity component, w, nondimensionalized using the Kolmogorov length and velocity scales, η and u_η. For reference, the figure also includes one-dimensional spectra of incompressible flows from DNS of HIT[26] and experiments of a boundary layer[27,28] and grid turbulence.[29]

the wavenumber vector, respectively.). Here, we instead present one-dimensional longitudinal spectra, such as $E_{ww}(k_z)$, because this representation is commonly used in experiments and allows direct comparison with available laboratory reference data in the same format. Owing to statistical isotropy, the one-dimensional longitudinal spectra along different Cartesian directions are equivalent up to statistical uncertainty, and the use of (w, k_z) is adopted as a representative choice. Accordingly, comparing DNS and experimental spectra on the same one-dimensional basis provides a consistent benchmark for assessing inertial-range-like behavior and high-wavenumber trends across datasets. The corresponding spectra of the solenoidal and dilatational components, $E_{ww,s}(k_z)$ and $E_{ww,d}(k_z)$, are shown in Fig. 3. For consistency, η and u_η computed from the total velocity field are used to nondimensionalize all spectra.

The spectra of the total velocity and the solenoidal component exhibit a slope close to $-5/3$ at low wavenumbers, consistent with inertial-range behavior and with the reference one-dimensional spectra of incompressible flows from DNS of HIT[26] and experiments of a boundary layer[27,28] and grid turbulence.[29] At high wavenumbers, the total spectrum increases with increasing M_{T0}. This trend is primarily due to the dilatational component: $E_{ww,d}(k_z)$ is enhanced at high wavenumbers as M_{T0} increases, which elevates the total spectrum in that range. These observations are consistent with previous results for stationary compress-

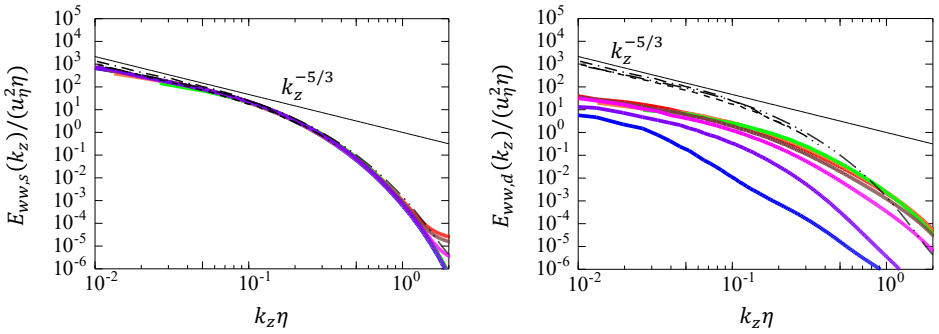

(a) (b)

FIG. 3: One-dimensional longitudinal energy spectra of (a) the solenoidal and (b) the dilatational components of the velocity field, nondimensionalized using η and u_η. The reference spectra and plotting conventions are the same as in Fig. 2. The line styles are also the same as in Fig. 2.

ible isotropic turbulence.[19,30] Having characterized how compressibility redistributes kinetic energy across scales, we now examine how these changes manifest in the nondimensional dissipation rate and its solenoidal and dilatational contributions.

2. *Nondimensional dissipation rate*

To quantify the sampling used for the global statistics, we compute each global quantity from a full-domain spatial average and then perform an ensemble average over five snapshots. Using the integral time scale defined from the target values, $T_0 = L_0/u_0$, the spacing between consecutive snapshots is approximately $0.45T_0$ and the total sampling window spans about $1.85T_0$. While this time record is not long enough to assess convergence by long-time averaging, the statistics at each snapshot are supported by full-domain spatial averaging over a large number of grid points in a triply periodic domain. As an uncertainty indicator, the snapshot-to-snapshot variability can be used to estimate the standard error of the global averages based on the five realizations. For the local conditional statistics, partitioning the domain into many subdomains provides a large number of local realizations for the conditioning/binned averages, thereby improving the robustness of the inferred scaling

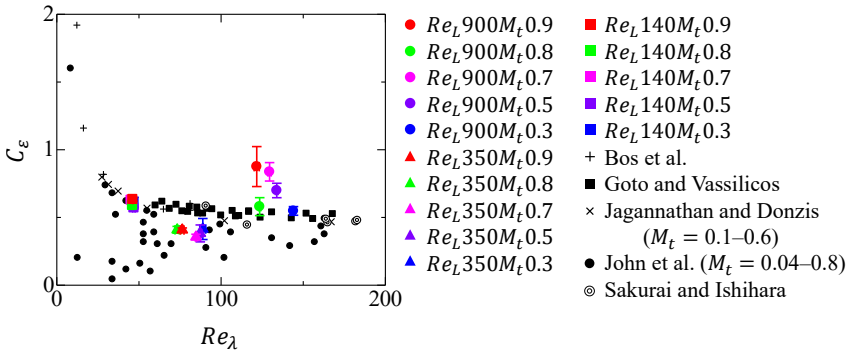

FIG. 4: Global nondimensional dissipation rate C_ε as a function of the turbulent Reynolds number Re_λ. The present DNS results are compared with reference data.[16,19,31,32] Error bars indicate the standard error estimated from the snapshot-to-snapshot variability among the five sampled times (ensemble average of five full-domain spatial averages).

trends, even though each subdomain average involves fewer grid points than the full-domain average.

Figure 4 shows the global nondimensional dissipation rate C_ε as a function of the turbulent Reynolds number Re_λ, together with reference data from previous studies.[16,19,31,32] For $Re_{L0} = 140$ and 350, the present results show that C_ε is nearly independent of Re_λ, consistent with the reference trends. In contrast, for $Re_{L0} = 900$, C_ε generally attains larger values and exhibits relatively large scatter. As shown later, however, this potential lack of convergence does not affect the local analysis, which is the primary focus of this study.

Next, we examine dissipation associated with the solenoidal and dilatational velocity components. We first consider the one-point solenoidal and dilatational dissipation rates, $\varepsilon_s(\boldsymbol{x})$ and $\varepsilon_d(\boldsymbol{x})$. Here and in what follows, $(\boldsymbol{x})$ denotes a one-point (local) quantity, whereas the same symbol without $(\boldsymbol{x})$ denotes the corresponding ensemble average. The solenoidal dissipation is computed analogously to the total dissipation, $\varepsilon(\boldsymbol{x}) = \tau_{ij}s_{ij}/(\rho Re)$, as

$$\varepsilon_s(\boldsymbol{x}) = \frac{1}{\rho Re}\tau_{sij}s_{sij}. \tag{22}$$

Here, τ_{sij} and s_{sij} are the viscous stress tensor and the strain-rate tensor, respectively, computed using the solenoidal velocity component. For the dilatational component, we compute

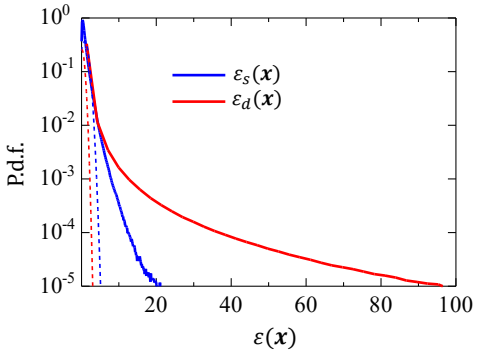

FIG. 5: Probability density functions of the solenoidal and dilatational dissipation rates, $\varepsilon_s(\boldsymbol{x})$ and $\varepsilon_d(\boldsymbol{x})$ for the case $Re_{L0} = 900$ and $M_{T0} = 0.9$. Dotted curves show Gaussian distributions with the same mean and variance as the corresponding data.

the compressive (bulk) contribution as

$$\varepsilon_d(\boldsymbol{x}) = \frac{4}{3}\frac{\mu}{\rho Re}\left(\frac{\partial u_j}{\partial x_j}\right)^2 . \tag{23}$$

Note that a strict solenoidal–dilatational decomposition of viscous dissipation in compressible turbulence may involve cross terms, so that $\varepsilon(\boldsymbol{x}) = \varepsilon_s(\boldsymbol{x}) + \varepsilon_d(\boldsymbol{x})$ does not necessarily hold pointwise. Here, Eq. (23) is used as a practical measure of the bulk (dilatational) contribution associated with velocity divergence, rather than as an exact energetic partition of $\varepsilon(\boldsymbol{x})$. Cross terms that may arise in a strict solenoidal–dilatational decomposition can, in principle, modify the quantitative partitioning between ε_s and ε_d and thus affect the absolute level of $C_{\varepsilon d}$. Nevertheless, the scaling tendencies emphasized in the present study are expected to be insensitive to this approximation, because Eq. (23) is directly controlled by $(\nabla\cdot\boldsymbol{u})^2$ and therefore captures the intermittent compressive events that dominate the strongest dilatational activity in our DNS. Accordingly, our main interpretation of the dilatational contribution focuses on the roles of local compressibility measures (e.g., M_t and M_{td}) and on the localization of large $\varepsilon_d(\boldsymbol{x})$ in strongly compressive regions, rather than on an exact energetic identity $\varepsilon = \varepsilon_s + \varepsilon_d$ at the pointwise level. A fully exact energetic partition including possible cross terms would be an interesting topic for future work, but is beyond the scope of the present analysis.

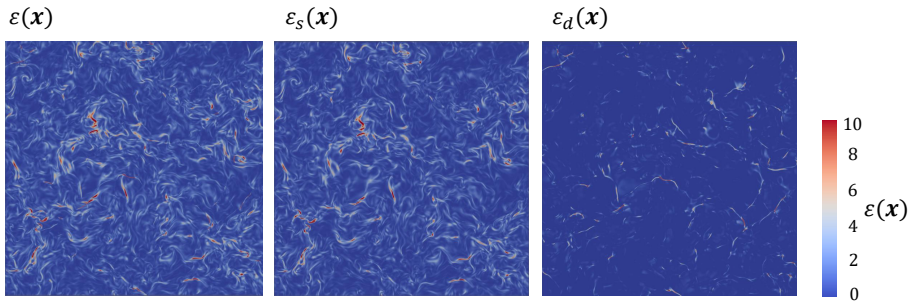

(a) (b) (c)

FIG. 6: Visualization of (a) total, (b) solenoidal, and (c) dilatational dissipation rates on a yz plane for the case $Re_{L0} = 900$ and $M_{T0} = 0.9$.

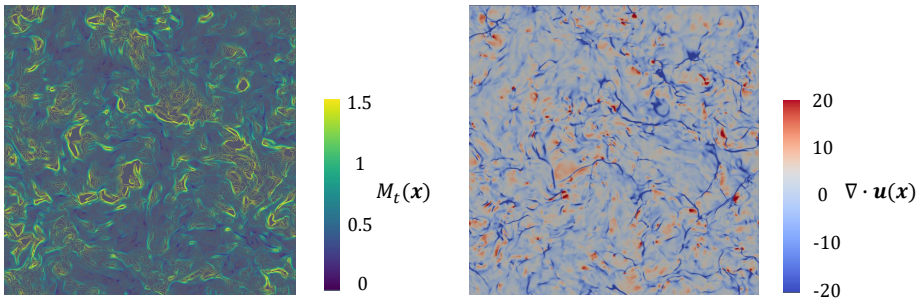

(a) (b)

FIG. 7: Visualization of (a) the local turbulent Mach number $M_t(\boldsymbol{x})$ and (b) the local velocity divergence $\nabla \cdot \boldsymbol{u}(\boldsymbol{x})$ on a yz plane for the case $Re_{L0} = 900$ and $M_{T0} = 0.9$.

Figure 5 shows probability density functions (PDFs) of the one-point solenoidal and dilatational dissipation rates, $\varepsilon_s(\boldsymbol{x})$ and $\varepsilon_d(\boldsymbol{x})$. In Fig. 5, the dotted curves indicate Gaussian distributions with the same mean and variance as the corresponding data. The PDF of $\varepsilon_d(\boldsymbol{x})$ exhibits a heavier tail toward large values than that of $\varepsilon_s(\boldsymbol{x})$, indicating that the dilatational dissipation is more intermittent and can attain much larger local magnitudes than the solenoidal dissipation.

Figure 6 visualizes the dissipation fields on a yz plane for the case $Re_{L0} = 900$ and

$M_{T0} = 0.9$. The solenoidal dissipation $\varepsilon_s(\boldsymbol{x})$ exhibits spatial features similar to those of the total dissipation $\varepsilon(\boldsymbol{x})$, whereas the dilatational dissipation $\varepsilon_d(\boldsymbol{x})$ forms more localized and intense structures. This observation is consistent with the PDFs in Fig. 5, which show a heavier tail for $\varepsilon_d(\boldsymbol{x})$. Figure 7 shows the corresponding fields of the local turbulent Mach number $M_t(\boldsymbol{x})$ and the velocity divergence $\nabla\cdot\boldsymbol{u}(\boldsymbol{x})$ on the same yz plane. The local turbulent Mach number is defined analogously to Eq. (7), but using one-point quantities based on the three-component velocity fluctuations. Comparing Figs. 6 and 7, regions of large $\varepsilon_d(\boldsymbol{x})$ tend to coincide with elevated $M_t(\boldsymbol{x})$ and with strongly compressive events (large negative $\nabla\cdot\boldsymbol{u}(\boldsymbol{x})$), suggesting that dilatational dissipation is amplified by compressibility and is associated with shocklet-like structures.

These localized coincidences between large $\varepsilon_d(\boldsymbol{x})$, elevated $M_t(\boldsymbol{x})$, and strong negative $\nabla\cdot\boldsymbol{u}(\boldsymbol{x})$ are consistent with the interpretation that intermittent compressive events produce sharp gradients and thereby activate compressible dissipation pathways. In particular, because $\varepsilon_d(\boldsymbol{x}) \propto (\nabla\cdot\boldsymbol{u})^2$, shocklet-like compressive events with large $|\nabla\cdot\boldsymbol{u}|$ directly yield intense, spatially localized dilatational dissipation. Such a gradient-driven intensification of nonequilibrium activity around mesoscale interfaces/structures has been emphasized, for example, in discrete Boltzmann studies of compressible Rayleigh–Taylor instability, where nonequilibrium measures peak near interfaces with strong macroscopic gradients and are generally enhanced as compressibility increases.[33,34] More broadly, multiscale discrete Boltzmann modeling of high-speed compressible flows shows that strong nonequilibrium effects become prominent around shock-related mesoscale structures, reflecting the role of rapid compression/expansion in amplifying transport and dissipation contributions.[35] Note that the term "nonequilibrium" in Refs. 33–35 refers to thermodynamic/kinetic nonequilibrium in the discrete-Boltzmann sense, which is distinct from the "nonequilibrium dissipation" terminology used here for the Reynolds-number dependence of C_ε. While the present HIT does not contain a persistent mean shock, the observed shocklet-like events play an analogous role by locally intensifying dilatational motions and hence the dilatational contribution to dissipation.

The solenoidal and dilatational dissipation coefficients, $C_{\varepsilon s}$ and $C_{\varepsilon d}$, are defined analogously to C_ε but are evaluated using the corresponding velocity component (solenoidal or

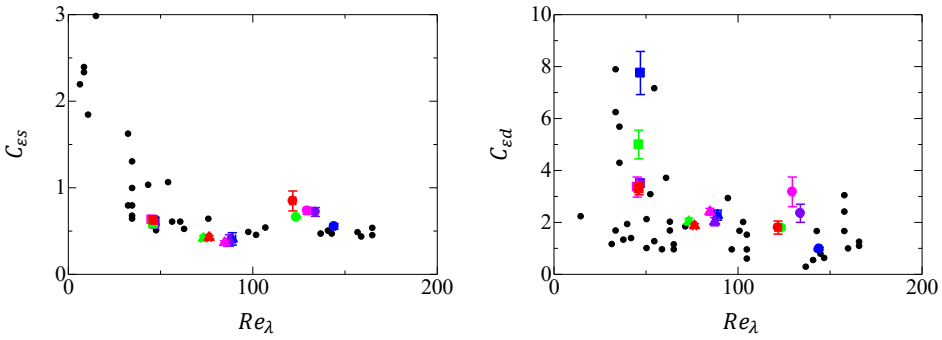

(a) (b)

FIG. 8: Global nondimensional dissipation rates of (a) the solenoidal component $C_{\varepsilon s}$ and (b) the dilatational component $C_{\varepsilon d}$ as functions of Re_λ. The symbols are the same as in Fig. 4. Error bars indicate the standard error estimated from the snapshot-to-snapshot variability among the five sampled times.

dilatational) together with its associated integral length scale and dissipation rate, i.e.,

$$C_{\varepsilon s} = \frac{\varepsilon_s L_s}{u_{sk,\mathrm{rms}}^3}, \quad C_{\varepsilon d} = \frac{\varepsilon_d L_d}{u_{dk,\mathrm{rms}}^3}. \tag{24}$$

Here, $u_{sk,\mathrm{rms}}$ and $u_{dk,\mathrm{rms}}$ denote the solenoidal and dilatational r.m.s. velocities, respectively, defined analogously to Eq. (19) using the solenoidal and dilatational velocity components. Comparing Fig. 4 (total) and Fig. 8(a) (solenoidal component) shows that the Re_λ dependence of $C_{\varepsilon s}$ closely mirrors that of the total C_ε. Figure 8(b) shows the corresponding dilatational coefficient $C_{\varepsilon d}$ as a function of Re_λ. When plotted against Re_λ, $C_{\varepsilon d}$ exhibits large scatter [Fig. 8(b)], a feature also reported by John et al.[16] As shown later, this scatter is markedly reduced in the local analysis, where conditioning on the local flow state decreases variability. Despite the scatter, $C_{\varepsilon d}$ shows an overall decreasing trend with increasing Re_λ.

To examine Reynolds-number measures appropriate for each component, we plot $C_{\varepsilon s}$ against the solenoidal turbulent Reynolds number $Re_{\lambda s}$ and $C_{\varepsilon d}$ against the corresponding dilatational value $Re_{\lambda d}$ in Figs. 9(a) and (b), respectively. Here, $Re_{\lambda s}$ and $Re_{\lambda d}$ are defined in the same manner as Re_λ, but are evaluated using the corresponding velocity component (solenoidal or dilatational) and its associated Taylor microscale, i.e., $Re_{\lambda s} = \langle\rho\rangle u_{sk,\mathrm{rms}}\lambda_s Re/\langle\mu\rangle$ and $Re_{\lambda d} = \langle\rho\rangle u_{dk,\mathrm{rms}}\lambda_d Re/\langle\mu\rangle$. Figure 9(a) shows that the trend of $C_{\varepsilon s}$

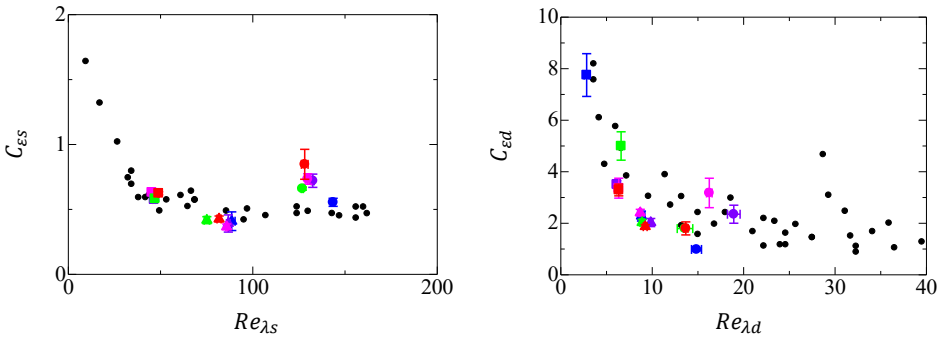

(a) (b)

FIG. 9: Global nondimensional dissipation rates plotted against component-based turbulent Reynolds numbers: (a) $C_{\varepsilon s}$ vs. $Re_{\lambda s}$ and (b) $C_{\varepsilon d}$ vs. $Re_{\lambda d}$. The symbols are the same as in Fig. 4. Error bars indicate the standard error estimated from the snapshot-to-snapshot variability among the five sampled times.

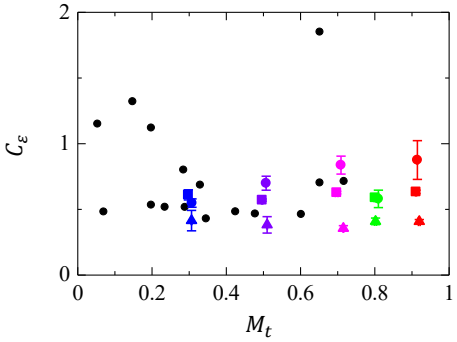

FIG. 10: Global nondimensional dissipation rate C_ε as a function of the turbulent Mach number M_t. The symbols are the same as in Fig. 4. Error bars indicate the standard error estimated from the snapshot-to-snapshot variability among the five sampled times.

with $Re_{\lambda s}$ is similar to that with Re_λ. In contrast, Fig. 9(b) indicates that $C_{\varepsilon d}$ collapses better when plotted against $Re_{\lambda d}$ than against Re_λ [cf. Fig. 8(b)]. Specifically, $C_{\varepsilon d}$ decreases with increasing $Re_{\lambda d}$ and tends toward an approximately constant value at sufficiently large $Re_{\lambda d}$.

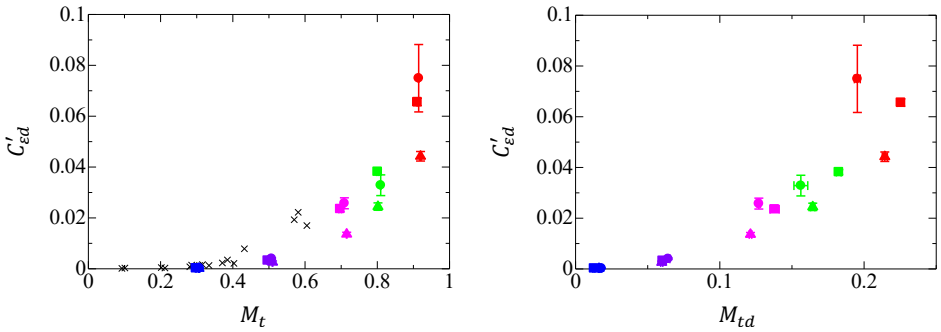

FIG. 11: Global dilatational dissipation measure $C'_{\varepsilon d} = \varepsilon_d L/u_{\rm rms}^3$ plotted against (a) M_t and (b) the dilatational turbulent Mach number M_{td}. The symbols are the same as in Fig. 4. Error bars indicate the standard error estimated from the snapshot-to-snapshot variability among the five sampled times.

Compressibility may influence the nondimensional dissipation rate through the dilatational contribution, and therefore through the turbulent Mach number M_t. Figure 10 shows C_ε as a function of M_t. Overall, C_ε exhibits only a weak dependence on M_t, and the variation becomes particularly small at larger M_t. The present results are consistent with previously reported trends. The scatter seen in global statistics is markedly reduced in the local analysis, as shown later. To isolate the Mach-number dependence of the dilatational dissipation, we also examine the normalization introduced by Jagannathan and Donzis[19]:

$$C'_{\varepsilon d} = \frac{\varepsilon_d L}{u_{\rm rms}^3}, \tag{25}$$

where L and $u_{\rm rms}$ are based on the total velocity fluctuations. Figure 11(a) shows that $C'_{\varepsilon d}$ increases with increasing M_t, consistent with Ref. 19. Figure 11(b) plots $C'_{\varepsilon d}$ against M_{td}. Here, the dilatational turbulent Mach number M_{td} is defined analogously to Eq. (21), but using the r.m.s. dilatational velocity fluctuations. A similar increasing trend is observed, reflecting the growth of dilatational motions with increasing compressibility. As shown later, however, the corresponding local relationships differ substantially from these global trends.

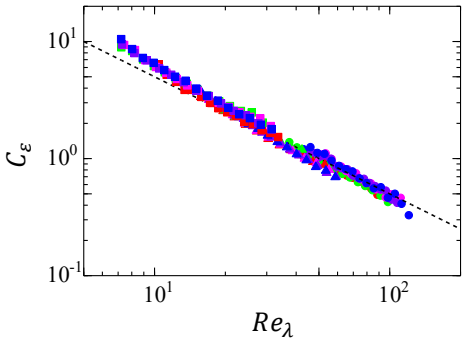

FIG. 12: Conditional averages of C_ε as a function of the locally evaluated Re_λ for all cases. The dotted line indicates a slope of -1. The symbols are the same as in Fig. 4.

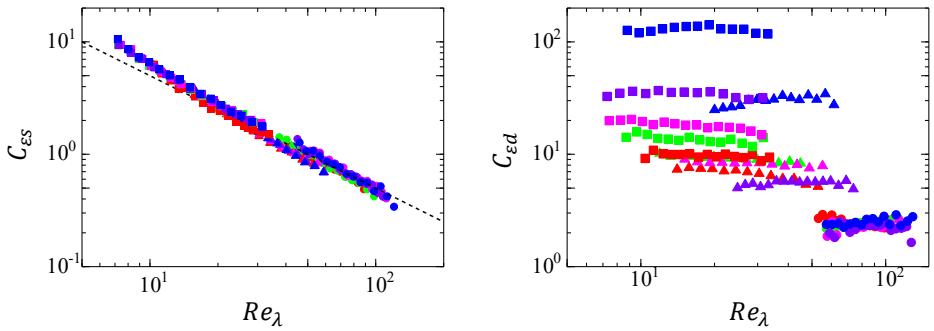

(a) (b)

FIG. 13: Conditional averages of (a) $C_{\varepsilon s}$ and (b) $C_{\varepsilon d}$ as functions of the locally evaluated Re_λ for all cases. The dotted line in (a) indicates a slope of -1. The symbols are the same as in Fig. 4.

B. Local-scale statistics

Figure 12 shows conditional averages of C_ε as a function of the locally evaluated Re_λ for all cases. All data collapse onto an approximately single straight line on the log–log plot with a slope close to -1, providing clear evidence of nonequilibrium scaling, $C_\varepsilon \sim Re_\lambda^{-1}$, at spatially local scales. We note that the global-to-local difference does not imply that

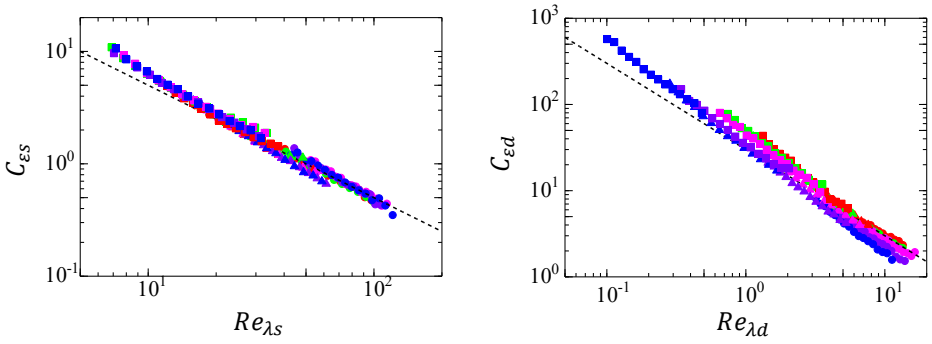

(a) (b)

FIG. 14: Conditional averages of (a) $C_{\varepsilon s}$ conditioned on $Re_{\lambda s}$ and (b) $C_{\varepsilon d}$ conditioned on $Re_{\lambda d}$ for all cases. The dotted lines indicate a slope of -1. The symbols are the same as in Fig. 4.

Re_λ is irrelevant. Rather, global averaging can mask local dependences in the presence of strong spatio-temporal intermittency. To clarify the role of Re_λ as a governing parameter, we emphasize that the local and global dissipation coefficients are defined through different averaging operations. The global coefficient is evaluated from globally averaged quantities, whereas the local coefficient is formed within each subdomain using local velocity and length scales and is then averaged or conditionally averaged. Because the normalization involves nonlinear combinations of fluctuating quantities, averaging and normalization are not commutative in general, and therefore an average (or spatial integration) of the locally defined C_ε is not expected to exactly recover the global value in principle. In this context, Re_λ is used as an effective similarity parameter for organizing the local dissipation statistics, particularly for the solenoidal (vortical) contribution, while compressibility effects are expected to enter primarily through dilatational dynamics and are better characterized by Mach-number measures, as examined below.

Figure 13 shows the corresponding conditional averages of the solenoidal and dilatational contributions, $C_{\varepsilon s}$ and $C_{\varepsilon d}$. As in the global statistics, the profiles of C_ε and $C_{\varepsilon s}$ are similar, whereas $C_{\varepsilon d}$ is nearly independent of the local Re_λ. Figure 14(a) shows $C_{\varepsilon s}$ conditioned on the solenoidal turbulent Reynolds number $Re_{\lambda s}$. The resulting profiles are very similar to those obtained when conditioning on Re_λ, indicating that the solenoidal scaling is insensitive

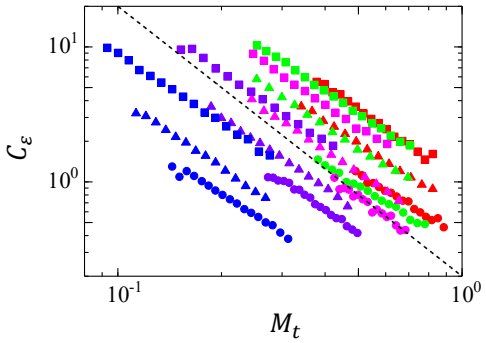

FIG. 15: Conditional averages of C_ε as a function of the locally evaluated M_t for all cases. The dotted line indicates a slope of -2. The symbols are the same as in Fig. 4.

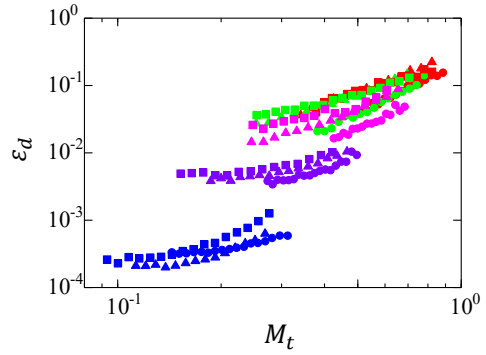

FIG. 16: Conditional averages of ε_d as a function of the locally evaluated M_t for all cases. The symbols are the same as in Fig. 4.

to the specific Reynolds-number definition used here. In contrast, Fig. 14(b) shows that the dilatational dissipation collapses when conditioned on $Re_{\lambda d}$ and follows a clear scaling, $C_{\varepsilon d} \sim Re_{\lambda d}^{-1}$.

We next examine the dependence on the local Mach number. Figure 15 shows conditional averages of C_ε as a function of the locally evaluated M_t for all cases. Overall, C_ε decreases with increasing M_t and approximately follows a slope close to -2. Unlike the Re_λ dependence in Fig. 12, however, the data do not collapse. This lack of collapse suggests that M_t alone is not an appropriate similarity parameter for the total dissipation. Instead, compressibility

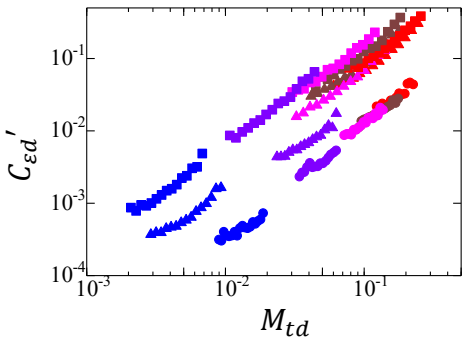

FIG. 17: Conditional averages of $C'_{\varepsilon d} = \varepsilon_d L/u_{\rm rms}^3$ as a function of the locally evaluated M_{td} for all cases. The symbols are the same as in Fig. 4.

effects are expected to enter primarily through the dilatational dissipation, which should correlate more directly with M_t. This expectation is supported by Fig. 16, which shows the conditional averages of ε_d as a function of M_t. Motivated by the global analysis in Fig. 11, we therefore examine the dilatational dissipation measure $C'_{\varepsilon d}$ as a function of the dilatational turbulent Mach number M_{td}. Figure 17 shows that $C'_{\varepsilon d}$ increases monotonically with M_{td} in the local analysis. This trend is consistent with the corresponding global relationship and contrasts with the Reynolds-number dependence, which differs markedly between global and local statistics.

IV. CONCLUSIONS

We investigated nonequilibrium dissipation scaling in compressible HIT using a direct numerical simulation database sustained by solenoidal linear forcing. The integral-scale Reynolds numbers were $Re_{L0} = 140$, 350, and 900, and the turbulent Mach number spanned $M_{T0} = 0.3$–0.9 in each Reynolds-number set. To isolate compressibility effects, we decomposed the velocity field into solenoidal and dilatational components via the Helmholtz decomposition and evaluated the corresponding dissipation measures both globally and locally. For the local analysis, the triply periodic domain was partitioned into non-overlapping cubic subdomains with side length of the order of the integral length scale, and conditional averages were computed using locally evaluated flow quantities.

Energy spectra confirmed inertial-range-like behavior for the total and solenoidal velocity fields, with a slope close to $-5/3$ at low wavenumbers. At high wavenumbers, the total spectrum increased with increasing M_{T0} at fixed Re_{L0}, primarily due to an enhancement of the dilatational spectrum. The one-point statistics further showed that the dilatational dissipation exhibits stronger intermittency than the solenoidal dissipation, with intense localized events associated with large negative velocity divergence and elevated local turbulent Mach number.

Global statistics showed that C_ε is nearly independent of Re_λ at $Re_{L0} = 140$ and 350, consistent with reference trends, although C_ε at $Re_{L0} = 900$ generally attains larger values and exhibits relatively large scatter. The solenoidal dissipation coefficient $C_{\varepsilon s}$ closely mirrored the behavior of the total C_ε when plotted against Re_λ, whereas the dilatational coefficient $C_{\varepsilon d}$ displayed substantial scatter in global plots. When plotted against component-based Reynolds numbers, $C_{\varepsilon d}$ collapsed more clearly with $Re_{\lambda d}$ and tended toward an approximately constant value at sufficiently large $Re_{\lambda d}$. Consistent with previous work, the dilatational dissipation measure $C'_{\varepsilon d}$ increased with increasing M_t and with the dilatational turbulent Mach number M_{td}.

The central result of this work is obtained from the local-scale analysis. Because the aforementioned global trends can be obscured by spatio-temporal intermittency, we therefore focus on subdomain-based local statistics that condition on the instantaneous local flow state. Conditional averages of the local dissipation coefficient collapsed across all cases when plotted against the local Taylor–microscale Reynolds number, yielding a clear nonequilibrium scaling, $C_\varepsilon \sim Re_\lambda^{-1}$. The solenoidal contribution exhibited the same nonequilibrium scaling, $C_{\varepsilon s} \sim Re_\lambda^{-1}$, and this result was insensitive to whether conditioning was performed using Re_λ or $Re_{\lambda s}$. In contrast, the dilatational contribution was nearly independent of the local Re_λ when conditioned on Re_λ, indicating that Reynolds number alone does not control the dilatational dissipation at local scales. However, the dilatational dissipation collapsed when conditioned on $Re_{\lambda d}$ and followed $C_{\varepsilon d} \sim Re_{\lambda d}^{-1}$.

Local conditioning on Mach number revealed a qualitatively different behavior from Reynolds-number conditioning. Although C_ε decreased with increasing local M_t, the data did not collapse, suggesting that M_t alone is not an appropriate similarity parameter for the total dissipation. By contrast, the dilatational dissipation correlated strongly with compressibility: the conditional averages of ε_d increased with local M_t, and the dilatational dissipation

measure $C'_{\varepsilon d}$ increased monotonically with M_{td} in the local analysis. These results indicate that compressibility effects enter the dissipation dynamics primarily through dilatational motions and that the associated contribution is better characterized by local Mach-number measures than by Re_λ alone.

Overall, our findings demonstrate that nonequilibrium dissipation scaling is fundamentally local in compressible HIT and persists robustly in the total and solenoidal dissipation coefficients. At the same time, compressibility manifests itself mainly through intermittent, localized dilatational dissipation that is controlled by local compressibility measures rather than by the global Reynolds number. The present local framework provides a useful route for separating Reynolds-number and Mach-number effects and for interpreting dissipation scaling in compressible turbulence.

In summary, the present local results suggest that Reynolds-number effects primarily organize the solenoidal dissipation dynamics, whereas Mach-number effects enter predominantly through intermittent dilatational activity. We note that the present Reynolds- versus Mach-number role separation has been established within the parameter range explored here ($Re_L \simeq 140$–900 and $M_t \simeq 0.3$–0.9) and for the present solenoidal linear forcing with cooling. Several promising directions would be valuable for further confirmation and broader applicability, including extension to higher Reynolds numbers, an expanded Mach-number range (especially at higher compressibility where shocklets become more prominent), and alternative forcing strategies or flow configurations (e.g., shear and wall-bounded compressible turbulence). In addition, applying the same local, state-conditioned diagnostics to assess and guide turbulence-model development (e.g., LES/RANS closures) is a promising avenue enabled by the present framework. Such extensions would help assess the robustness of the local nonequilibrium scaling and further clarify the respective roles of Reynolds number and Mach number in other turbulent flows whenever sufficiently resolved local statistics are available. Importantly, while the present approach of local, state-conditioned statistics is transferable in spirit, its implementation in non-homogeneous flows requires appropriate adaptations, for example by using position-dependent reference scales and analysis volumes aligned with the relevant outer scales (e.g., wall distance or shear/shock length scales), rather than a uniform partition with a single global L. Moreover, in more realistic compressible turbulent flows, additional mechanisms—such as mean-shear production and anisotropy, wall friction and heat transfer, strong thermodynamic property variations, and persistent shock-induced

large gradients—may modify the quantitative scaling trends and the relative importance of solenoidal versus dilatational contributions. Accordingly, the present results should be viewed as a baseline established in solenoidally forced compressible HIT, and extensions to such flows would be valuable to assess how these additional effects reshape local dissipation scaling.

ACKNOWLEDGMENTS

The authors are grateful to the anonymous reviewers for their constructive and insightful comments, which helped improve the manuscript. This work was supported by JSPS KAKENHI Grant No. JP23K22669. The authors acknowledge the financial support by Research Institute for Mathematical Sciences, Kyoto University. The numerical simulations were performed using the high-performance computing systems at the Japan Agency for Marine-Earth Science and Technology and Nagoya University. This work was also supported by a Collaborative Research Project on Computer Science with High-Performance Computing in Nagoya University.

AUTHOR DECLARATIONS

Conflict of interest

The authors have no conflicts to disclose.

Author Contributions

Yohei Nishimoto: Data Curation (lead); Formal Analysis (lead); Investigation (equal); Methodology (equal); Validation (lead); Writing/Original Draft Preparation (lead); Writing/Review & Editing (equal). **Koji Nagata**: Conceptualization (lead); Formal Analysis (supporting); Funding Acquisition (lead); Investigation (lead); Methodology (lead); Project Administration (lead); Supervision (lead); Validation (equal); Writing/Original Draft Preparation (equal); Writing/Review & Editing (lead). **Tomoaki Watanabe**: Conceptualization (equal); Data Curation (equal); Formal Analysis (equal); Investigation (equal); Methodology (equal); Project Administration (equal); Resources (lead); Supervision (equal); Validation

Local nonequilibrium dissipation scaling in compressible homogeneous isotropic turbulence (supporting); Writing/Review & Editing (equal).

DATA AVAILABILITY

The data that support the findings of this study are available from the corresponding author upon reasonable request.

REFERENCES

[1]J. C. Vassilicos, "Dissipation in turbulent flows," Annual Review of Fluid Mechanics **47**, 95 (2015).

[2]A. N. Kolmogorov, "Dissipation of energy in the locally isotropic turbulence," Proceedings of the Royal Society of London. Series A: Mathematical and Physical Sciences **434**, 15 (1991).

[3]A. N. Kolmogorov, "On degeneration (decay) of isotropic turbulence in an incompressible viscous liquid," Dokl. Akad. Nauk SSSR **31**, 538 (1941).

[4]A. N. Kolmogorov, "The local structure of turbulence in incompressible viscous fluid for very large Reynolds numbers," Dokl. Akad. Nauk SSSR **30**, 301 (1941).

[5]K. R. Sreenivasan, "On the scaling of the turbulence energy dissipation rate," The Physics of Fluids **27**, 1048 (1984).

[6]K. R. Sreenivasan, "An update on the energy dissipation rate in isotropic turbulence," Physics of Fluids **10**, 528 (1998).

[7]T. Kitamura, K. Nagata, Y. Sakai, A. Sasoh, O. Terashima, H. Saito, and T. Harasaki, "On invariants in grid turbulence at moderate Reynolds numbers," Journal of Fluid Mechanics **738**, 378 (2014).

[8]L. Djenidi, N. Lefeuvre, M. Kamruzzaman, and R. Antonia, "On the normalized dissipation parameter in decaying turbulence," Journal of Fluid Mechanics **817**, 61 (2017).

[9]Y. Zheng, K. Nagata, and T. Watanabe, "Energy dissipation and enstrophy production/destruction at very low Reynolds numbers in the final stage of the transition period of decay in grid turbulence," Physics of Fluids **33**, 035147 (2021).

[10]R. Seoud and J. Vassilicos, "Dissipation and decay of fractal-generated turbulence," Physics of Fluids **19**, 105108 (2007).

[11]P. C. Valente and J. C. Vassilicos, "Universal dissipation scaling for nonequilibrium turbulence," Physical Review Letters **108**, 214503 (2012).

[12]R. J. Hearst and P. Lavoie, "Decay of turbulence generated by a square-fractal-element grid," Journal of Fluid Mechanics **741**, 567 (2014).

[13]K. Nagata, T. Saiki, Y. Sakai, Y. Ito, and K. Iwano, "Effects of grid geometry on non-equilibrium dissipation in grid turbulence," Physics of Fluids **29**, 015102 (2017).

[14]W. J. Bos and R. Rubinstein, "Dissipation in unsteady turbulence," Physical Review Fluids **2**, 022601 (2017).

[15]T. Kitamura, K. Nagata, K. Shimoyama, and T. Nanri, "On the normalised energy dissipation rate in homogeneous isotropic turbulence," Journal of Fluid Mechanics **1010**, A14 (2025).

[16]J. P. John, D. A. Donzis, and K. R. Sreenivasan, "Does dissipative anomaly hold for compressible turbulence?" Journal of Fluid Mechanics **920**, A20 (2021).

[17]H. Aluie, "Compressible turbulence: The cascade and its locality," Physical Review Letters **106**, 174502 (2011).

[18]B. R. Pearson, T. A. Yousef, N. E. L. Haugen, A. Brandenburg, and P.-Å. Krogstad, "Delayed correlation between turbulent energy injection and dissipation," Physical Review E **70**, 056301 (2004).

[19]S. Jagannathan and D. A. Donzis, "Reynolds and Mach number scaling in solenoidally-forced compressible turbulence using high-resolution direct numerical simulations," Journal of Fluid Mechanics **789**, 669 (2016).

[20]Y. Zheng, K. Nakamura, K. Nagata, and T. Watanabe, "Unsteady dissipation scaling in static-and active-grid turbulence," Journal of Fluid Mechanics **956**, A20 (2023).

[21]Y. Zheng, N. Koto, K. Nagata, and T. Watanabe, "Unsteady dissipation scaling of grid turbulence in the near-field region," Physics of Fluids **35**, 095131 (2023).

[22]T. Watanabe, K. Tanaka, and K. Nagata, "Solenoidal linear forcing for compressible, statistically steady, homogeneous isotropic turbulence with reduced turbulent mach number oscillation," Physics of Fluids **33**, 095108 (2021).

[23]K. Yamamoto, T. Ishida, T. Watanabe, and K. Nagata, "Experimental and numerical investigation of compressibility effects on velocity derivative flatness in turbulence," Physics of Fluids **34**, 055101 (2022).

[24]Y. Nishimoto, K. Nagata, T. Watanabe, and Y. Zhou, "Spatially local dissipation scaling in grid turbulence from direct numerical simulations." Physics of Fluids (2026), in press.

[25]T. Watanabe, C. B. Da Silva, and K. Nagata, "Non-dimensional energy dissipation rate near the turbulent/non-turbulent interfacial layer in free shear flows and shear free turbulence," Journal of Fluid Mechanics **875**, 321 (2019).

[26]T. Watanabe and K. Nagata, "The response of small-scale shear layers to perturbations in turbulence," Journal of Fluid Mechanics **963**, A31 (2023).

[27]S. G. Saddoughi and S. V. Veeravalli, "Local isotropy in turbulent boundary layers at high Reynolds number," Journal of Fluid Mechanics **268**, 333 (1994).

[28]F. T. M. Nieuwstadt, J. Westerweel, and B. Boersma, *Turbulence: Introduction to Theory and Applications of Turbulent Flows*, 1st ed. (Springer, Cham, 2016).

[29]A. L. Kistler and T. Vrebalovich, "Grid turbulence at large Reynolds numbers," Journal of Fluid Mechanics **26**, 37 (1966).

[30]H. Yang, H. Yan, J. Wu, H. Wang, D. Yu, X. Li, and J. Wang, "Kinetic energy spectrum and transfer within the near-dissipation range of compressible isotropic turbulence," Physics of Fluids **37**, 015182 (2025).

[31]W. J. Bos, L. Shao, and J.-P. Bertoglio, "Spectral imbalance and the normalized dissipation rate of turbulence," Physics of Fluids **19**, 045101 (2007).

[32]S. Goto and J. Vassilicos, "The dissipation rate coefficient of turbulence is not universal and depends on the internal stagnation point structure," Physics of Fluids **21**, 035104 (2009).

[33]H. Lai, A. Xu, G. Zhang, Y. Gan, Y. Ying, and S. Succi, "Nonequilibrium thermohydrodynamic effects on the Rayleigh–Taylor instability in compressible flows," Physical Review E **94**, 023106 (2016).

[34]H. Lai, C. Lin, Y. Gan, D. Li, and L. Chen, "The influences of acceleration on compressible Rayleigh–Taylor instability with non-equilibrium effects," Computers & Fluids **266**, 106037 (2023).

[35]Q. Guo, Y. Gan, B. Yang, Y. Wu, H. Lai, and A. Xu, "Thermodynamic nonequilibrium effects in three-dimensional high-speed compressible flows: Multiscale modeling and simulation via the discrete Boltzmann method," Physics of Fluids **37**, 046117 (2025).